Eur. Phys. J. B **3**, 185–188 (1998)

THE EUROPEAN PHYSICAL JOURNAL B

Magnetic phase diagram of perovskite Mn oxides at T = 0

Y. Liu[1], J. Dong[2,a], and D.Y. Xing[3]

[1] Department of Physics, Nanjing University, Nanjing 210008, P.R. China
[2] National Laboratory of Solid State Microstructures, Nanjing University, Nanjing 210008, P.R. China
[3] Center for Advanced Studies in Science and Technology of Microstructures, Nanjing 210093, P.R. China

Received: 11 July 1996 / Revised: 7 December 1996 / Accepted: 24 July 1997

Abstract. Minimizing total free energy by numerical calculations, we obtain the magnetic phase diagram of perovskite Mn oxides, such as $(La_{1-x}X_x)MnO_3$ with X = Ba, Ca, Sr, *etc.* in the whole doping region from $x = 0$ to $x = 1$ at temperature $T = 0$. It is discovered that a spiral state is stable in a low concentration of X ions while a canted state is stable in a high concentration of X ions, and a ferromagnetic phase can exist in the intermediate concentrations when the antiferromagnetic interaction is weak. The energy difference between spiral and canted states is found to be small when the Hund coupling is large. Magnetic field induced spiral/canted phase transition is considered as a possible mechanism of the colossal magnetoresistance (CMR) in the Mn oxides.

PACS. 71.27.+a Strongly correlated electron systems; heavy fermions – 72.15.Gd Galvanomagnetic and other magnetotransport effects – 75.10.-b General theory and models of magnetic ordering

1 Introduction

Perovskite Mn oxides, $(La_{1-x}X_x)MnO_3$ with X = Ba, Ca, Sr, *etc.* have recently attracted considerable attention because of a huge negative magnetoresistance (colossal magnetoresistance or CMR) near room temperature [1–7]. The resistivity drop due to an external magnetic field is usually much larger than that observed in magnetic multilayers [8]. MR amplitude $\Delta R/R(H)$ as large as 10^6 has been reported for (Pr-Ca)MnO_3 [9]. So high a MR is believed to be due to an insulator-metal transition caused by the magnetic field.

It is well known that $(La_{1-x}X_x)MnO_3$ are materials in which an antiferromagnetic (AF) insulator phase at $x = 0$ changes to a metallic ferromagnetic (FM) phase for $0.2 \leq x \leq 0.5$ [10]. Appearance of the metallic ferromagnetism on doping has been explained by the mechanism of the double exchange interactions [11,12]. The Mn^{3+} ions in $LaMnO_3$ have four d shell eletrons, with three electrons in the t_{2g} state as localized spins of $S = 3/2$ and one electrons in the e_g state as itinerant electron of $S = 1/2$ due to the Hund coupling. Because of the strong Hund coupling and on-site Coulomb repulsion between e_g electrons, $LaMnO_3$ is an antiferromagnetic insulator. By substituting X atoms for La atoms, Mn^{3+} ions change to Mn^{4+} ions with three localized electrons but none itinerant electron. The appearance of Mn^{4+} ions in $(La_{1-x}X_x)MnO_3$ introduces mobile carriers (holes) into the Hubbard subband. The vacant e_g state of Mn^{4+} makes it possible for e_g electrons in surrounding Mn^{3+} ions to hop into the e_g state of Mn^{4+} ions so long as the t_{2g} spins of the neighboring Mn^{3+} and Mn^{4+} ions are parallel. Thus a competition appears between a gain in the kinetic energy and a loss in the exchange energy of t_{2g} spins which favor antiferromagnetic coupling. With increasing number of mobile carriers on further doping of X atoms, the gain in the kinetic energy overcomes the loss of the exchange energy, which results in a transition to metallic ferromagnetism around $x \sim 0.2$.

Despite the long history of work on these materials, however, the magnetic phase diagram of the Mn oxides in the whole region with x from 0 to 1 is not completely clear. A competition between the kinetic and exchange energies led to the prediction of existence of the canted (CN) ferromagnetism for $0 < x < 0.2$ [13], while a spiral (SP) state is recently demonstrated to be more stable [14]. Further investigations on the magnetic phase diagram are then needed. Based up on the model Hamiltonian in [14], we make a numerical calculation and obtain a phase diagram covering the whole region of x. It is shown that, with increasing of holes, an AF state at $x = 0$ changes first into a SP state, subsequently into a FM state, then a CN state, and finally returns to an AF state at $x = 1$. The energy difference between SP state and CN state is found to be in inverse proportion to the strength of Hund coupling. A magnetic field can change easily a SP state into a CN state rather than into a FM state. The SP/CN phase transition due to applied magnetic field provides a plausible mechanism accounting for the CMR effect of the perovskite Mn oxides.

[a] e-mail: zyq@netra.nju.edu.cn

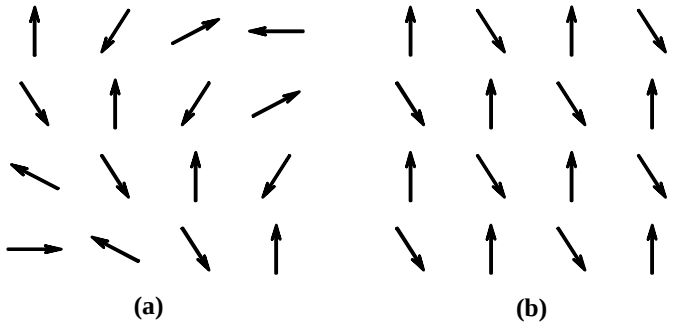

Fig. 1. Schematic illustrations of two-dimensional (1,1) SP state (a) and CN state (b).

This paper is organized in the following way. In Section 2, model Hamiltonian is introduced and an expression of free energy is given. The numerical results and discussions are given in Section 3. The final section is the summary.

2 Theoretical description

Including only Mn ions and neglecting effect of the other atoms, we can obtain a model Hamiltonian in which the correlated itinerant electrons couple with the localized spins by a strong Hund coupling. Thus the Hamiltonian is given by

$$H = -t\sum_{\langle ij\rangle\sigma} a^{\dagger}_{i\sigma}a_{j\sigma} + \sum_{i\sigma}\epsilon_0 a^{\dagger}_{i\sigma}a_{i\sigma} + \frac{U}{2}\sum_{i\sigma} n_{i\sigma}n_{i\bar{\sigma}} + J\sum_{\langle ij\rangle}\mathbf{S}_i\,\mathbf{S}_j - \frac{K}{2}\sum_i \mathbf{S}_i\,\boldsymbol{\sigma}_i. \quad (1)$$

Here, $t(>0)$ denotes the transfer integral of itinerant electrons between nearest-neighbor (NN) sites,ϵ_0 the on-site potential of itinerant electrons, U the on-site Coulomb repulsion between $\uparrow$ and $\downarrow$ spin itinerant electrons, $a^{\dagger}_{i\sigma}(a_{i\sigma})$ is a creation (an annihilation) operator of an itinerant electron at site i with spin σ, $n_{i\sigma} = a^{\dagger}_{i\sigma}a_{i\sigma}$, $J(>0)$ is the NN exchange interaction between localized spins, $K(>0)$ represents the Hund coupling, and $\boldsymbol{\sigma}$ stands for the Pauli matrix.

We apply the Hartree-Fock approximation to the Hamiltonian and consider SP state and CN state respectively. The illustrations for two-dimensional (1,1) SP and CN states are shown in Figure 1. In our coordinate system, the z-axis is taken to be perpendicular to all the spins, and the direction of spin on site i can be denoted by its spherical coordinate $(\pi/2, \varphi_i)$. The relative angle between two nearest neighbouring spins on sites i and j is $\varphi_{ij} = \varphi_i - \varphi_j$. Its absolute value $|\varphi_{ij}|$ is independent of i and j and can be denoted as $\pi + 2\theta$ (with 2θ the canting angle). In order to determine the spin configurations completely, we have to identify the signs of φ_{ij}. In SP state, the signs depend only on the relative displacements $\mathbf{R}_{ij} = \mathbf{R}_i - \mathbf{R}_j$, and for any site i, we can write

$$\varphi_{ij} = \begin{cases} \pi + 2\theta, & \text{for } \mathbf{R}_{ij} = \hat{\mathbf{x}}, \hat{\mathbf{y}} \\ -(\pi + 2\theta), & \text{for } \mathbf{R}_{ij} = -\hat{\mathbf{x}}, -\hat{\mathbf{y}}. \end{cases}$$

For CN state, we divide all sites into two sublattices so that all the nearest neighbours of each site in sublattice A belong to sublattice B, and *vice versa* for sublattice B. The signs of φ_{ij} in CN state rely on the i being in the sublattice A or B:

$$\varphi_{ij} = \begin{cases} \pi + 2\theta, & \text{for } i\in A \\ -(\pi + 2\theta), & \text{for } i\in B \end{cases}$$

for all the nearest neighbours j of site i. Obviously, both SP and CN state become AF state or FM state respectively as θ goes to 0 or $\pi/2$.

After decoupling the quartic Hund coupling term by HFA, we will have the term $\boldsymbol{\sigma}_i\langle\mathbf{S}_i\rangle$, which depends explicitly on the orientation of $\langle\mathbf{S}_i\rangle$. This is not convenient for further calculations, because the orientation of $\langle\mathbf{S}_i\rangle$ varies from site to site. Therefore, we take the spin quantization axis at each site to be along $\langle\mathbf{S}_i\rangle$, *i.e.*, using a set of local spin quantization axes. Rotation of spin quantization axes from original fixed one to the set of local ones is equivalent to a unitary transformation of the Hamiltonian,

$$a_{i\uparrow} = e^{-i\varphi_i/2}(c_{i\uparrow} + c_{i\downarrow})/\sqrt{2},$$
$$a_{i\downarrow} = e^{i\varphi_i/2}(c_{i\uparrow} - c_{i\downarrow})/\sqrt{2}. \quad (2)$$

By the transformation, our Hamiltonian is reduced to be

$$H = E_0 + H_d + H_s, \quad (3)$$

where E_0 is the constant term, H_d is the Hamiltonian of local spins, and H_s is the Hamiltonian of itinerant electrons, with

$$E_0 = -NUn_{\uparrow}n_{\downarrow} - J\sum_{\langle ij\rangle}\langle\mathbf{S}_i\rangle\langle\mathbf{S}_j\rangle + (K/2)\sum_i\langle\mathbf{S}_i\rangle\langle\boldsymbol{\sigma}_i\rangle, \quad (4)$$

$$H_d = \sum_i \langle\mathbf{L}_i\rangle\mathbf{S}_i, \quad (5)$$

and

$$H_s = -t\sum_{\langle ij\rangle\sigma}[\cos(\varphi_{ij}/2)c^{\dagger}_{i\sigma}c_{j\sigma} + i\sin(\varphi_{ij}/2)c^{\dagger}_{i\sigma}c_{j\bar{\sigma}}] + \sum_{i\sigma} v_\sigma c^{\dagger}_{i\sigma}c_{i\sigma}. \quad (6)$$

Here, $\mathbf{L}_i = 2J\sum_{j\neq i}\mathbf{S}_j - K\boldsymbol{\sigma}_i/2$, $v_\sigma = \epsilon_0 + Un_{\bar{\sigma}} - \sigma K|\langle\mathbf{S}_i\rangle|/2$, $n_\sigma = \langle c^{\dagger}_{i\sigma}c_{i\sigma}\rangle$ is the electron density, with $\sigma = \uparrow$ or $\downarrow$. We next diagonalize the Hamiltonian H_s by considering SP state and CN state, respectively.

For the (1,1,1) SP state with a propagation wave vector $\pi + 2\theta$, and by Fourier transformation, equation (6) becomes

$$H_s = \sum_{\mathbf{k}\sigma}[(v_\sigma - \epsilon_{\mathbf{k}}\sin\theta)c^{\dagger}_{\mathbf{k}\sigma}c_{\mathbf{k}\sigma} - \epsilon'_{\mathbf{k}}\cos\theta c^{\dagger}_{\mathbf{k}\sigma}c_{\mathbf{k}\bar{\sigma}}]. \quad (7)$$

Here, $\epsilon_{\mathbf{k}} = -2t\sum_{l=1}^{d}\cos k_l$, $\epsilon_{\mathbf{k}}^{'} = 2t\sum_{l=1}^{d}\sin k_l$, d denotes the dimensionality. Introducing new Fermi operators $d_{\mathbf{k}\uparrow}$ and $d_{\mathbf{k}\downarrow}$ in terms of the relations

$$c_{\mathbf{k}\uparrow} = [U_+(\xi)d_{\mathbf{k}\uparrow} + (\epsilon_{\mathbf{k}}/|\epsilon_{\mathbf{k}}|)U_-(\xi)d_{\mathbf{k}\downarrow}]/\sqrt{2},$$
$$c_{\mathbf{k}\downarrow} = [(\epsilon_{\mathbf{k}}/|\epsilon_{\mathbf{k}}|)U_-(\xi)d_{\mathbf{k}\uparrow} - U_+(\xi)d_{\mathbf{k}\downarrow}]/\sqrt{2}, \quad (8)$$

with $\xi = (1/2)\arctan[\Delta_E/|\epsilon_{\mathbf{k}}^{'}|\cos\theta]$, and $U_\pm(\xi) = |\sin\xi \pm \cos\xi|/\sqrt{2}$, the Hamiltonian is diagonalized as

$$H_s = \sum_{\mathbf{k}}[E_-^{SP}(\mathbf{k})d_{\mathbf{k}\uparrow}^\dagger d_{\mathbf{k}\uparrow} + E_+^{SP}(\mathbf{k})d_{\mathbf{k}\downarrow}^\dagger d_{\mathbf{k}\downarrow}], \quad (9)$$

where

$$E_\pm^{SP}(\mathbf{k}) = v_0 - \epsilon_{\mathbf{k}}\sin\theta \pm (\Delta_E^2 + \epsilon_{\mathbf{k}}^{'2}\cos^2\theta)^{\frac{1}{2}}, \quad (10)$$

with $v_0 = (v_\downarrow + v_\uparrow)/2$ being the normalized on-site potential, and $\Delta_E = (v_\downarrow - v_\uparrow)/2$ being the effective field, which represents the strength of Hund coupling.

For the CN state with two sublattices, the Fourier transform of equation (6) is derived to be

$$H_s = \sum_{\mathbf{k}\sigma}[(v_\sigma - \epsilon_{\mathbf{k}}\sin\theta)c_{\mathbf{k}\sigma}^\dagger c_{\mathbf{k}\sigma} + i\epsilon_{\mathbf{k}}\cos\theta c_{\mathbf{k}\sigma}^\dagger c_{\tilde{\mathbf{k}}\bar{\sigma}}], \quad (11)$$

where $\tilde{\mathbf{k}}$ is the reduced wave-vector corresponding to $\mathbf{k} + \mathbf{k}_0/2$, and $\mathbf{k}_0 = (\sum_{l=1}^{d}\hat{\mathbf{b}}_l)$ with $\hat{\mathbf{b}}_l$ the basis vectors of the reciprocal lattice. Note that $\epsilon_{\tilde{\mathbf{k}}} = -\epsilon_{\mathbf{k}}$. In equation (11), two single-particle states with momentum $\mathbf{k}$ and $\tilde{\mathbf{k}}$ and opposite spins are coupled. By using the unitary transformation

$$c_{\mathbf{k}\uparrow} = [U_+(\chi)d_{\mathbf{k}\uparrow} + i(\epsilon_{\mathbf{k}}/|\epsilon_{\mathbf{k}}|)U_-(\chi)d_{\tilde{\mathbf{k}}\downarrow}]/\sqrt{2},$$
$$c_{\tilde{\mathbf{k}}\downarrow} = [i(\epsilon_{\mathbf{k}}/|\epsilon_{\mathbf{k}}|)U_-(\chi)d_{\mathbf{k}\uparrow} + U_+(\chi)d_{\tilde{\mathbf{k}}\downarrow}]/\sqrt{2}, \quad (12)$$

with $\chi = (1/2)\arctan[(\Delta_E - \epsilon_{\mathbf{k}}\sin\theta)/|\epsilon_{\mathbf{k}}|\cos\theta]$, and $U_\pm(\chi) = |\sin\chi \pm \cos\chi|/\sqrt{2}$, the Hamiltonian is diagonalized as

$$H_s = \sum_{\mathbf{k}}[E_-^{CN}(\mathbf{k})d_{\mathbf{k}\uparrow}^\dagger d_{\mathbf{k}\uparrow} + E_+^{CN}(\mathbf{k})d_{\tilde{\mathbf{k}}\downarrow}^\dagger d_{\tilde{\mathbf{k}}\downarrow}], \quad (13)$$

where

$$E_\pm^{CN}(\mathbf{k}) = v_0 \pm (\Delta_E^2 + \epsilon_{\mathbf{k}}{}^2 \pm 2\Delta_E\epsilon_{\mathbf{k}}\sin\theta)^{\frac{1}{2}}. \quad (14)$$

Our results (Eqs. (10, 14)) recover the equations (2, 3) in [14]. The results are also valid for two-dimensional (1,1) SP and CN states as well as for one-dimensional states. The eigenvalues of AF and FM states are correctly obtained in the limits of $\theta = 0$ and $\theta = \pi/2$, respectively.

In determining phase diagram, only the ratios K/t and J/t *etc.* are of significance, so we can let $t = 1$ for convenience. As we know, hole number per site in Mn ions equals to the doping concentration x, so $n_\uparrow + n_\downarrow = 1 - x$. At $T = 0\,\mathrm{K}$, the total free energy per site is

$$F(\theta) = -2dJS^2\cos(2\theta) + \frac{1}{N}\sum_{\mathbf{k}}[E_-f(E_-) + E_+f(E_+)], \quad (15)$$

with $f(\epsilon) = \theta(\mu - \epsilon)$, the Fermi-Dirac distribution function. Here, N is the total number of the lattice sites, and $\mathbf{k}$ is the wave vectors. The first term in equation (15) is the free energy of local spins. The chemical potential μ is determined from the condition of fixed density:

$$1 - x = \frac{1}{N}\sum_{\mathbf{k}}[f(E_-) + f(E_+)], \quad (16)$$

From equations (15, 16), we calculate the total free energies of SP state and CN state in the whole $x - JS^2$ plane respectively. By comparing the total free energies with respect to θ at fixed x, we get the minimal free energies, and then obtain the phase diagram.

3 Numerical results

When $T = 0\,\mathrm{K}$, only the lower energy branch $E_-(\mathbf{k})$ is occupied by the carriers. So we merely consider the lower branch in calculating the free energy of the itinerant electrons. Then equation (15) changes to be

$$F(\theta) = -2dJS^2\cos(2\theta) + \frac{1}{N}\sum_{\mathbf{k}}E_-f(E_-), \quad (17)$$

and equation (16) changes to be

$$1 - x = \frac{1}{N}\sum_{\mathbf{k}}f(E_-), \quad (18)$$

with

$$E_-^{SP}(\mathbf{k}) = v_0 - \epsilon_{\mathbf{k}}\sin\theta - (\Delta_E^2 + \epsilon_{\mathbf{k}}^{'2}\cos^2\theta)^{\frac{1}{2}}, \quad (19)$$

$$E_-^{CN}(\mathbf{k}) = v_0 - (\Delta_E^2 + \epsilon_{\mathbf{k}}{}^2 - 2\Delta_E\epsilon_{\mathbf{k}}\sin\theta)^{\frac{1}{2}}. \quad (20)$$

By assuming that $\Delta_E > 2dt$, which corresponds to the case of large Hund coupling, we calculate the free energies of SP state and CN state in two dimensions. Here, we let $\Delta_E = 5, 10, 20, 100$. Detailed process is as follows.

First, we let θ change from 0 to $\pi/2$, and using equations (19, 20), we obtain a series of values of $E_-^{SP}(\mathbf{k})$ and $E_-^{CN}(\mathbf{k})$ with different θ and $\mathbf{k}$. Second, giving values of x and JS^2 and using equation (18), we get the chemical potential μ. Substituting it into equation (17), we obtain the free energy $F(\theta)$. Thus, we get a minimal free energy with fixed θ and x. Third, let x change from 0 to 1, and repeating the above procedure, we obtain a series of minimal free energies $F_{min}(\theta)$ for SP state and CN state with different $x(0 \sim 1)$. Then, we compare the minimal free energies of SP state and CN state with fixed x. If $\theta = \pi/2$, we define the system is in FM state, and if $\theta = 0$, it is in AF state. If $\theta \neq 0$ and $\pi/2$, the system is in the state (SP or CN) whose minimal free energy $F_{min}(\theta)$ is lower. Finally, let JS^2 changes from 0 to a finite value, we obtain the magnetic phase diagrams at $T = 0\,\mathrm{K}$ for different Δ_E in the whole $x - JS^2$ plane (see Fig. 2).

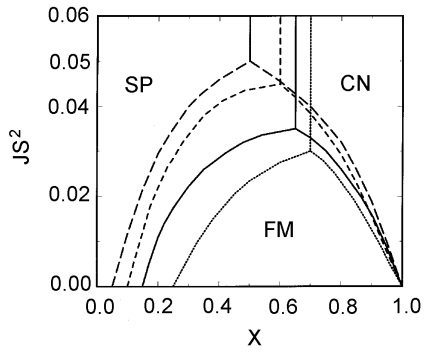

Fig. 2. Magnetic phase diagrams in $x - JS^2$ plane with different Δ_E at $T = 0K$. (a) $\Delta_E = 5$ (dot line), (b) $\Delta_E = 10$ (solid line), (c) $\Delta_E = 20$ (short-dashed line), (d) $\Delta_E = 100$ (long-dashed line).

In Figure 2, we can find that, when the antiferromagnetic interaction is weak (that means JS^2 is small), a FM phase can be found in the middle region of x. Strong Hund coupling gives rise to FM double exchange interaction, which competes with AF superexchange interaction and leads to AF/SP/FM/CN/AF or AF/SP/CN/AF phase transitions as x changes from 0 to 1. With increasing Δ_E, the area of FM phase in the whole phase diagram increases. When the antiferromagnetic interaction is strong enough (that means JS^2 is large enough), the FM phase disappears, and there are only SP and CN phases in the diagram. Moreover, the areas of SP and CN phases are not symmetric. It is obvious in Figure 2 that for lower Δ_E value, the SP phase has larger area in the phase diagram than the CN phase. With increasing Δ_E, the CN phase occupies more and more area, and the boundary line between the SP and CN phases moves to the left. Finally, for very large $\Delta_E \sim 100$, the line lies at $x = 0.5$. Especially, even in the absence of AF superexchange interaction ($JS^2 = 0$), x has to reach a certain value for appearance of the FM phase, and the critical value of x decreases with increasing Δ_E.

Now, we make a qualitative comment on the MR effects in Mn oxides. As we know, SP state has no net global magnetization, but CN state as well as FM state have global magnetizations of $M_s \sin\theta$ and M_s, respectively, with M_s the saturation magnetization. Thus, when the SP/CN or SP/FM phase transition occurs, there is usually a sudden increase of the global magnetization. When a small magnetic field **H** is applied, the CN state becomes more stable than SP state by an energy difference of $H(M_s/N)\sin\theta$ per site. And from our numerical results, the energy difference between SP state and CN state decreases while Δ_E increases (that means the Hund coupling is becoming stronger). So long as the energy difference caused by the magnetic field is larger than the energy difference between SP state and CN state without the magnetic field, a SP/CN phase transition can easily occur in the presence of the magnetic field. When in the CN state, the gain in the kinetic energy overcomes the loss of the exchange energy, and the carriers can move more easily than those in the SP state, then the conductivity increases drastically, leading to a huge negative MR. So we can conclude that the Hund coupling plays an important role for CMR in Mn oxides.

4 Summary

In summary, using numerical calculations to minimize the total free energy, we have obtained the magnetic phase diagram of the perovskite Mn oxides, such as $(La_{1-x}X_x)MnO_3$ with X = Ba, Ca, Sr, *etc.* in the whole region from $x = 0$ to $x = 1$ at $T = 0$. As it shows, the antiferromagnetism of $LaMnO_3$ first changes to the spiral state, not the canted state, on introducing mobile carriers into the Mn oxides. The canted state is shown to be favored in highly doped Mn oxides close to $x \sim 1$. It has been shown that, strong Hund coupling giving rise to FM double exchange interaction competes with AF superexchange interaction, which leads to AF/SP/FM/CN/AF or AF/SP/CN/AF phase transitions as x changes from 0 to 1. The CMR effect in Mn oxides can be interpreted qualitatively in terms of a magnetic field induced SP/CN phase transition.

One of the authors Y. Liu especially thanks Dr. Li Sheng for his thorough help.

References

1. G. Matsumoto, J. Phys. Soc. Jpn **29**, 606 (1970).
2. R.M. Kusters, J. Singleton, D.A. Keen, R. McGreevy, W. hayes, Physica **155B**, 362 (1989).
3. R. von Helmolt, L. Haupt, K. Barner, U. Sondermann, Solid Stat. Commun. **82**, 693 (1992).
4. R. von Helmolt, J. Wecker, B. Holzapfel, L. Schultz, K. Samwer, Phys. Rev. Lett. **71**, 2331 (1993).
5. K. Chahara, T. Ohno, M. Kasai, Y. Kozono, Appl. Phys. Lett. **63**, 1990 (1993).
6. M. McCormack, S. Jin, T.H. Tiefel, R.M. Fleming, J.M. Phillip, R. Ramech, Appl. Phys. Lett. **64**, 3045 (1994).
7. Y. Tokura, A. Urushibara, Y. Moritomo, T. Arima, A. Asamitsu, G. Kido, N. Furukawa, J. Phys. Soc. Jpn **63**, 3931 (1994).
8. M.N. Baibich, J.M. Broto, A. Fert, Nguyen Van Dau, F. Petroff, P. Eitenne, G. Creuzet, A. Friederich, J. Chazelas, Phys. Rev. Lett. **61**, 2472 (1988).
9. Y. Tomioka, A. Asamitsu, Y. Moritomo, Y. Tokura, to be published.
10. E.O. Wollen, W.C. Koehler, Phys. Rev. **100**, 545 (1955).
11. C. Zener, Phys. Rev. **82**, 403 (1951).
12. P.W. Anderson, H. Hasegawa, Phys. Rev. **100**, 675 (1955).
13. P.-G. de Gennes, Phys. Rev. **118**, 141 (1960).
14. J. Inoue, S. Maekawa, Phys. Rev. Lett. **74**, 3407 (1995).